Available online at www.sciencedirect.com

ScienceDirect

Advances in Space Research 75 (2025) 7610–7623

ADVANCES IN SPACE RESEARCH (a COSPAR publication)

www.elsevier.com/locate/asr

Modelling aerodynamic drag of a very low earth orbit 1U CubeSat utilising a Boltzmann-BGK approach

Joseff Parke Sturrock *, Ben Evans, Zoran Jelic

Bay Campus, Swansea University, Fabian Way, Swansea SA1 8EN, United Kingdom

Received 28 May 2024; received in revised form 20 March 2025; accepted 23 March 2025
Available online 26 March 2025

Abstract

The aerodynamic drag of a 1U CubeSat at various Very Low Earth Orbit (VLEO) altitudes and conditions have been investigated utilising an in-house Boltzmann-BGK solver. This region of space has numerous benefits, however significant drag can lead to short satellite lifespans. The analyses focus on determining drag coefficients, as well as absolute drag values. Flow fields are illustrated. Monoatomic oxygen number density ratios on exposed surfaces were presented to help guide corrosion analysis. Material properties for satellite surface coatings have been analysed, including drag reduction performance. All atmospheric parameters were sourced from NASA's NRLMSIS 2.0 atmospheric model. Altitudes investigated range from 50 km to 500 km. Periods of solar minima and maxima, seasonal variances and local day/night cases were investigated. Drag coefficients were evaluated and compared with corresponding Knudsen numbers. Although there are significant variations of the drag coefficient (C_D) at very low altitudes, higher altitudes produced consistent values. Two CubeSat geometric orientations were studied, one settled to a consistent C_D of around 1.24 for higher altitudes, while the other case settled to a C_D of 1.60. The material property of specularlity was found to have a considerable impact on drag coefficients – altering this parameter could lead to significantly higher drag coefficients, in some cases exceeding values of 2.0. The drag coefficients computed can be coupled with other existing models to determine satellite lifespan, as well as to estimate expected drag at various orbital altitudes. This will be insightful for determining thrust values of drag compensation systems, serving to extend the lifespan of VLEO operating satellites.

Keywords: CubeSat; Boltzmann-BGK; Rarefied Gas; Satellite Drag; Drag Compensation

1. Introduction

Very low Earth orbits (VLEO) are desirable regions for satellite operations for numerous reasons. Benefits include significantly improved pixel resolution of Earth observation instruments, exponentially reduced link budgets, end-of-life passive de-orbiting and a reduced orbital insertion altitude, effectively increasing launch vehicle payload mass – typically measured in $/kg to a higher altitude, stable low Earth orbit (Roberts, 2021). Additionally, VLEO allows for direct atmospheric sampling, above the maximum altitude of high-altitude weather balloons, granting access to regions of the atmosphere only currently accessible to short duration sounding rockets (Burth et al, 2023). Such regions of the upper mesosphere/lower thermosphere are undergoing climatic change (Cnossen, 2022).

The main engineering challenges of these regions are significant atmospheric drag. This results in rapid orbital decay, leading to very short satellite lifespan. Additionally, the number density of corrosive monoatomic oxygen is orders of magnitude higher than at higher altitude, stable orbits (Banks et al, 2019).

The focus of this work was to determine drag values and coefficients for sizing thrust values of a novel electric propulsion system. Compensating drag effectively counters

* Corresponding author.
E-mail address: 868466@swansea.ac.uk (J.P. Sturrock).

https://doi.org/10.1016/j.asr.2025.03.055
0273-1177/

orbital decay – allowing a stable orbit at altitudes that a satellite without propulsion would rapidly deorbit in. This has been demonstrated most effectively by JAXA's Super Low Altitude Test Satellite (SLATS), achieving a world record circular orbit of 167.4 km, for seven days, by compensating drag (JAXA, 2019, Kawasaki et al 2018). CubeSats are an attractive option for sampling altitudes even lower than this, due to their typically cheaper cost and shorter life span. This allows more insight when designing larger satellites, which require significantly more financial investment.

The results outlined within this paper were generated using an in-house Boltzmann-BGK rarefied gas solver (Evans et al, 2011, Evans and Walton, 2017, Evans 2018, Evans et al, 2019). The input data was sourced from NASA's NRLMSIS2.0 atmospheric model (Emmert et al, 2021, NASA, 2021). The default case was in a period of medium solar irradiance, 45° latitude (April 1st, 1970). This was used as a baseline case. Other variables were also investigated. This includes periods of solar minima and maxima, local day/night and local winter/summer. Latitudes of 0° and 90° were also evaluated. Studies evaluated the drag force, which was then used to determine two-dimensional drag coefficients and extrapolating to the three-dimensional drag force of a 1U CubeSat. Both on-axis and off-axis geometric orientations were studied.

To the authors best knowledge, this is the first work characterising drag coefficients of 1U CubeSats utilising a Boltzmann-BGK approach. A similar model has been applied to study re-entry conditions of a spherical spacecraft, as well as a re-entry capsule shaped geometry (Li and Zhang, 2009). That model showed strong agreement between computed results and experimental data, with the largest difference in computed drag coefficient being 5%, although typically the results were accurate to within 2% of the experimental data. Other Boltzmann-BGK models exist, including another investigation of a hypersonic re-entry cylinder's flow fields, but did not compute drag coefficients (Baranger et al, 2020). Another studied low density nozzle performances (Deng et al, 1995).

The Boltzmann-BGK approach was used to build upon previous experience within the research group, after multiple successful implementations of the solver in a wide range of applications. The solver has been previously validated with comparisons to other computational methods, such as molecular dynamics simulations, as well as analytical solutions (Evans, 2018, Evans et al, 2011, Evans et al 2008).

In existing literature, Direct Simulation Monte Carlo (DSMC) is the most common approach for computationally investigating CubeSat drag (Marín-Cebrián et al, 2019, Groesbeck et al, 2019, Sheridan et al, 2022). More detail is provided in Section 3.4, however employing a Boltzmann-BGK method is intended to complement existing drag predictions obtained via other methods. This aims to broaden the number of methods used in CubeSat drag estimates, acting as an alternative solution to DSMC, rather than a replacement.

2. Methodology

2.1. Background of model

The Boltzmann-BGK solver used in the studies has been in development since 2008 (Evans et al, 2008). For a complete breakdown of each algorithmic process, the reader is advised to refer to the previous publications of this model (Evans et al, 2011, Evans and Walton, 2017, Evans 2018, Evans et al, 2019). In the interest of conciseness, a summarised view of the solver will be described in this paper, condensed from previous works. The algorithm has previously been extensively described in multiple computational journals, so this paper focuses on the application specific results.

The atmospheric conditions of VLEO are considerably different from that of sea level. This is due to the many orders of magnitude lower mass density of the free stream. Classical aerodynamic models (such as Navier-Stokes) treat air as a continuous medium. This method relies on a very high rate of collisions between the atmosphere's constituent particles, which coalesce into familiar macroscopic phenomena, such as viscosity. At low densities, the physical distance between each particle is high. Thus, for a given temperature (a measure of the particles' average velocity), the rate of collisions is lower for a lower density fluid (Chapman and Cowling, 1990). This concept is denoted as the Mean Free Path (MFP) of a particle – the average distance a particle will travel before colliding with another. The larger the MFP, the lower the rate of collision events occur. Equation (1) describes the MFP of a fluid.

$$\lambda = \frac{k_B T}{\sqrt{2}\pi d^2 P} \tag{1}$$

where λ is the MFP, k_B is the Boltzmann constant, T is the free stream temperature, d is the diameter of the particle and P is free stream pressure. The dimensionless Knudsen number (Kn) is used to describe how a fluid may behave. It is defined as the ratio of the MFP to the reference length of the flow ($Kn = \lambda/L$). Where L is that length. As this paper focuses on 1U CubeSats, the reference length for all studies was 0.1 m. This is the side length of all standard 1U CubeSats. Fig. 1 shows which modelling approach may be used for a corresponding Kn value of a fluid flow problem.

Although the upper atmosphere is a dynamic region, subject to change from differing conditions (particularly the intensity of solar activity), the Knudsen number of a value equal to 1 was found at an altitude of 98 km for the default cases – just below the Kármán line. At this altitude, temperature was 181.6 K, pressure was 0.043 Pa and average molecular diameter was 3.51E-10 m, sourced from NRLMSIS 2.0 (Emmert et al, 2021). As such, all feasible orbital pathways studied (which receive acceptable levels of drag and thermal heating) have a Kn value greater than 1.0. Therefore, all continuum methods are invalid, and a Boltzmann approach is utilised. As $Kn \ll 100$ for some

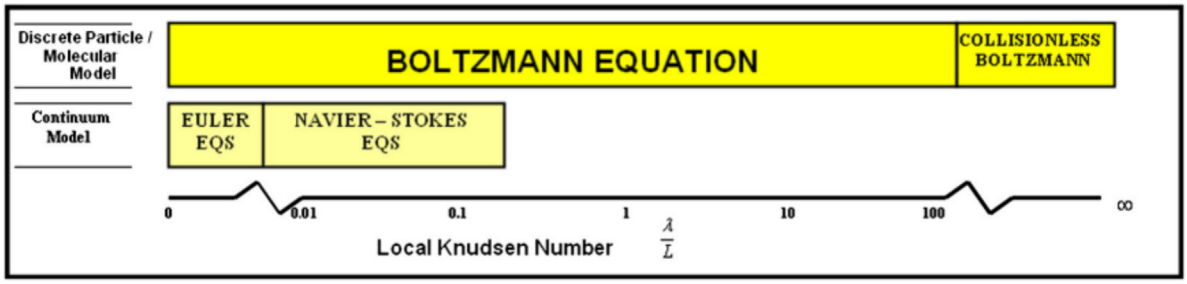

Fig. 1. The Knudsen Regime (Evans and Walton, 2017).

studies (as low as 9.0), the collisions of particles were included for all studies.

2.2. The BGK simplification to the Boltzmann approach

The full Boltzmann equation is as follows:

$$\frac{\partial(nf)}{\partial t} + \boldsymbol{c}\frac{\partial(nf)}{\partial \boldsymbol{r}} + \boldsymbol{F}\frac{\partial(nf)}{\partial \boldsymbol{c}} = \frac{1}{Kn}Q(f,f) \tag{2}$$

where n is the number density of particles, $f = f(\boldsymbol{r}, \boldsymbol{c}, t)$ is the distribution function, $\boldsymbol{F}$ describes all forces in the system (neglecting electrostatic forces for this purely aerodynamic model), and $\boldsymbol{c}$ is the molecular velocity vector. $Q(f,f)$ accounts for molecular collisions and is inherently complex (Harris, 1971). This complexity requires the need of simplification when modelling non-trivial applications, allowing simulations to be resolved with acceptable computational resource. The simplification of choice for the solver used for this paper is the Bhatnagar, Gross and Krook (BGK) assumption (Bhatnagar et al, 1954). The resulting Boltzmann-BGK equation becomes:

$$\frac{\partial(nf)}{\partial t} + \boldsymbol{c}\frac{\partial(nf)}{\partial \boldsymbol{r}} + \boldsymbol{F}\frac{\partial(nf)}{\partial \boldsymbol{c}} = v(\boldsymbol{r},t)((nf_0) - (nf)) \tag{3}$$

where $v(\boldsymbol{r},t)$ is a term proportional to particle collision frequency and f_0 is the local Maxwellian equilibrium distribution function:

$$f_0(\boldsymbol{c}) = \left(\frac{\beta^3}{\pi^{1.5}}\right)\exp\left(-\beta^2(\boldsymbol{c}-\boldsymbol{c}_0)^2\right) \tag{4}$$

where $\boldsymbol{c}_0$ is the bulk velocity of the flow and $\beta = \sqrt{m/(2k_BT)}$, where m is molecular mass. This simplification is significantly computationally cheaper to perform when compared to the unmodified Boltzmann equation.

2.3. Discretisation of the simulated domain

The domain is discretised in both the physical space, as well as velocity space. This is due to the velocity distribution function encompassing both these domains. The physical space, Ω_r, is discretised into discontinuous, unstructured and triangular elements. The discontinuity allows for phenomena such as shock waves to be observed. This solver is in two dimensions of physical space. Additionally, the velocity space domain is also discretised. Although theoretically this velocity space would encompass up to light speed, no particles are expected to approach close to relativistic velocities. As such, an upper limit was placed on the velocity space, r_v. For this work, that value was set to 13,000 ms^{-1}, nearly double the free stream. A previous publication of this solver, analysing a hypersonic re-entry vehicle (exhibiting similar free stream parameters), found this level to be representative (Evans and Walton, 2017). Despite an artificial limit placed on maximum particle velocity, this assumption (saving significant computational expense) has negligible effect on total bulk flow properties, as any particles travelling faster than this limit are a very insignificant fraction compared to the bulk. Fig. 2 depicts the discretised physical and velocity spaces.

Further detail into the governing equations, Lobatto quadrature weighting scheme, discontinuous Taylor-Galerkin approach, inflow and outflow methods, as well as boundary condition applications can be found in the previous publications in computational journals (Evans et al, 2011, Evans and Walton, 2017, Evans 2018, Evans et al, 2019).

2.4. Computational domain

The chosen domain size was 1 m x 1 m, so that the 0. 1 m x 0.1 m CubeSat was occupying 1% of the total domain's area. Due to the relatively low number of particle collisions, the free stream parameters at the edge of the domain were almost always near identical to the input free stream properties. This was due to the lack of collisions reducing the ability of perturbations to propagate far from the geometry. With a higher altitude, collisions become less frequent, so this becomes more pronounced. Fig. 3 illustrates the mesh used for these studies, increasing in detail, from the whole domain to the boundary layers.

All cases were conducted on an in-house high-performance computing cluster, using 160 cores per simulation. High order parallelisation was utilised, as described in previous works (Evans et al, 2019). The algorithm is iterative, and all cases were run until drag values converged to

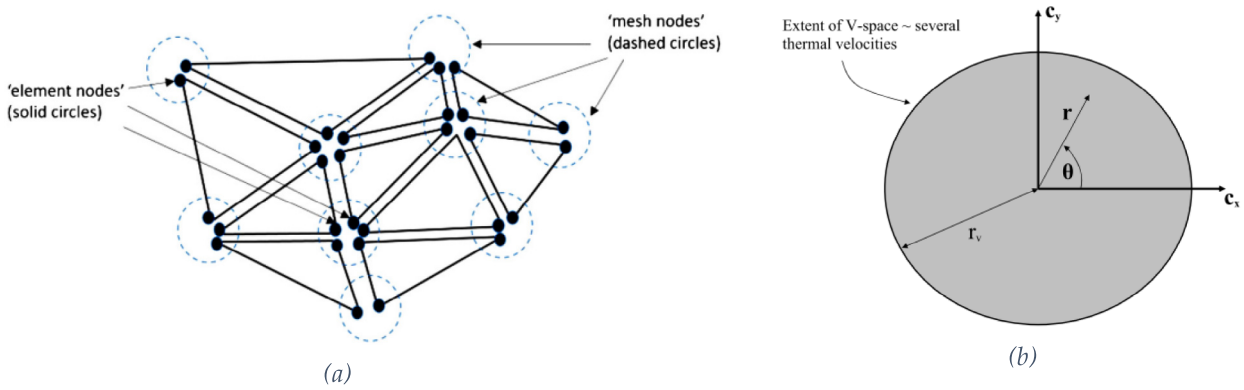

Fig. 2. Simulated Domain. (a) Discontinuous, unstructured, triangular elements for the discretisation of physical space. (b) Velocity space domain. (Evans and Walton, 2017).

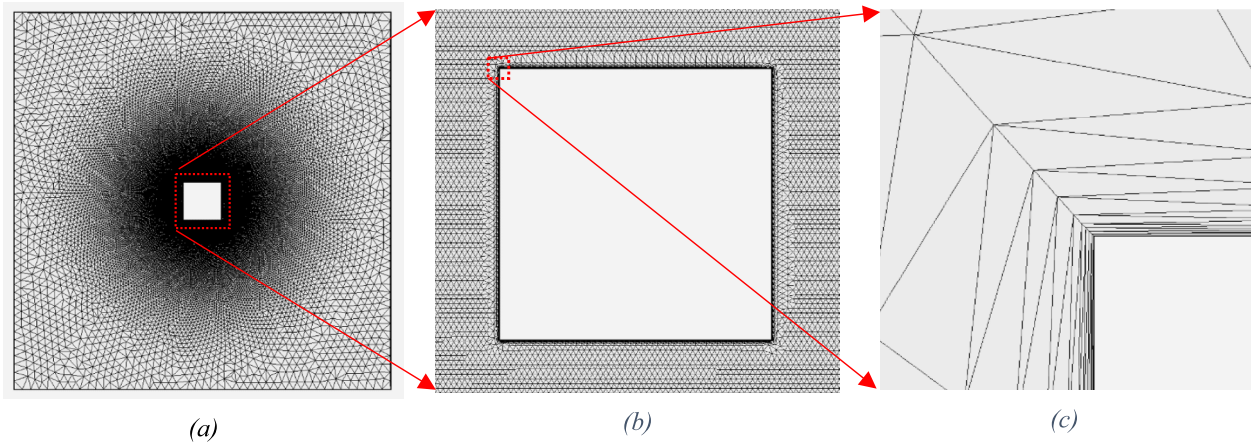

Fig. 3. Physical space mesh for the 1U CubeSat, on-axis case: (a) full domain, (b) CubeSat geometry, (c) boundary layers.

steady state (four significant figures). Run times were typically around 48 h. Output values were post-processed using Ensight, a visualisation software.

2.5. Modifying the free stream composition and molecular wall reflection parameter

The primary differences between the studies conducted for this paper, versus previous publications, was the varying composition of the free stream atmosphere, modelling various molar fractions of the expected free stream molecular species. Parameters such as number density, temperature and pressure were sourced from NRLMSIS 2.0, and a simple circular orbit velocity computation was used for free stream velocity (Emmert et al, 2021). The equation for this velocity is $v = \sqrt{GM/r}$, where G is the gravitational constant, M is the mass of Earth, and r is the radius of the circular orbit. The parameter for molecular diameter, d, was input on every study. This was calculated as an average value, based upon the corresponding case's molar fractions of each type of molecule's individual diameter. The average molar mass (again utilising the known molar fractions of each case) was also input, with units of daltons. This allowed for calculating the specific gas constant, R, for each case too.

Monoatomic oxygen number densities were evaluated using Ensight. Number densities of these species were computed for the exposed surfaces of the CubeSat. The leading edge produced the highest number densities – they were evaluated as a multiple of free stream monoatomic oxygen number density.

As incident particles impact the walls of the spacecraft, they are reflected. This reflection can be treated as either specular or diffuse. Specular reflection occurs when the angle of reflection is equal to the angle of incidence, whereas in diffuse reflection, the angle of reflection differs from the angle of incidence. Fig. 4 shows these two interactions.

A critical parameter in the algorithm is the molecular wall reflection parameter, α, which describes the fraction of molecules that are specularly reflected versus diffusely reflected. This value was set to 0.9 for the default cases. This means that 90% of the molecules were modelled as reflecting specularly, whereas the other 10% were reflected

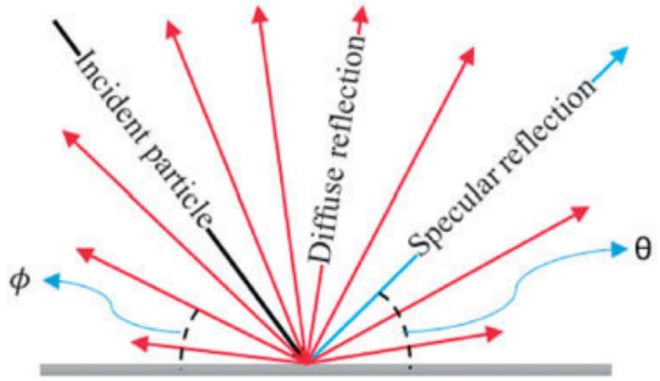

Fig. 4. Specular Deflection (Blue) versus Diffuse Reflection (Red) (Bahmani and Nazif, 2019).

diffusely. This ratio was found to be most representative for previous studies that the model had been applied to.

Despite this – there are many coatings that exist or are under development for satellite surfaces, to increase the fraction of molecules that are specularly reflected. This reduces drag and crucially, helps reduce monoatomic oxygen corrosion (Banks et al, 2019). As such, a case study was also conducted – varying α by increments of 0.1, from 0.1 to 0.9. A best-case scenario of $\alpha = 0.99$ was also conducted. This will allow for satellite surface coatings with a known α to be compared with the simulation results, as a guideline for the impact of how much a specific coating's α may affect drag and monoatomic oxygen corrosion.

3. Results and discussion

3.1. Default case and atmospheric composition

The chosen default case was 1st April, 00:00, 1970. Latitude 45° and longitude 180°. This date was chosen to satisfy several conditions. Firstly, the year corresponded to a period of medium solar irradiance. This allowed for the solar minima/maxima to be referenced to the mid-case. The same principle was applied to the month, being neither local summer, nor winter. Again, these seasonal variances were investigated, with April being a chosen mid-ground. The period of midnight was also used for the default case. This is because the influence of charged particles from solar wind is reduced. As this is a purely aerodynamic model, the effects of plasma were not considered. As such, the default case was conducted during night, to reduce these unsimulated influences. The latitude of 45° was again consistent as neither being an equatorial nor polar extreme. Those locations were also simulated. The longitude was arbitrarily chosen as 180°. This corresponds with a position north of the centre of the Pacific Ocean, which may help reduce any effects that could be caused by mountainous topography.

Using the NRLMSIS 2.0 data table, molar components of the atmosphere were recorded, as well as number density, temperature and mass density. Pressure was also calculated using the ideal gas law, utilising the average molar mass (Emmert et al, 2021). Fig. 5 is an illustration of how molar fractions of the atmosphere change with altitude. This is for the default case, altitudes from 0 km to 700 km.

N2 is for diatomic nitrogen molecules, O2 is diatomic oxygen, N1 represents monoatomic nitrogen, O1 is monoatomic oxygen, He are helium atoms and Ar are argon atoms. Finally, H1 represents monoatomic hydrogen. At altitudes above 100 km, monoatomic oxygen becomes a significant fraction. At altitudes above 190 km, it is the most common species, being near total for altitudes corresponding with 300 – 600 km.

Fig. 6 shows the mass density of the atmosphere versus altitude for the default case, as well as the average molecular diameter of that altitude's atmospheric composition.

Despite being a very low density when compared with lower altitudes, drag is still significant. As the aerodynamic drag is governed by $D = 0.5 C_D \rho_\infty v_\infty^2 S$, where D is drag, C_D is the drag coefficient, ρ_∞ is atmospheric mass density, v_∞ is free stream velocity and S is frontal area (0.01 m^2 for the 1U CubeSat). Although for an altitude of 150 km, mass density of the atmosphere is only 2E-9 kg m^{-3}, the orbital velocity of a satellite, around 7800 ms^{-1}, means that the term ρv^2 is on the order of 0.001. Therefore, drag values for these altitudes were computed to be on the millinewton level. For the default case, this altitude's drag was computed to be 0.7 mN. Assuming a circular orbit, this drag would act constantly, resulting in impulses that would require large amounts of propellant to compensate for a sustained period of time. As such, cold gas or chemical micro-propulsion systems designed for CubeSats would be unsuitable, necessitating the need for higher specific impulse electric propulsion units, such as ionic liquid electrospray thrusters (Lemmer, 2017).

3.2. Flow fields and atomic oxygen ratios

The flow fields were visualised using Ensight at various altitudes. Fig. 7 shows the distribution of the number density of the surrounding atmosphere of a 1U CubeSat in the default case, of both the on-axis and off-axis cases.

At altitudes below 100 km, corresponding with the near-continuum Knudsen regime, classical high-speed aerodynamic phenomena can be observed, such as shockwaves. At altitudes of 100 km and above, where the Knudsen number is approximately one, these phenomena were no longer present due to the too large mean free path. The reduced particle collisions were the cause of this. The reduced collisions result in the higher altitude cases having a more one-dimensional distribution (along the direction of travel). Very low number densities were observed in the

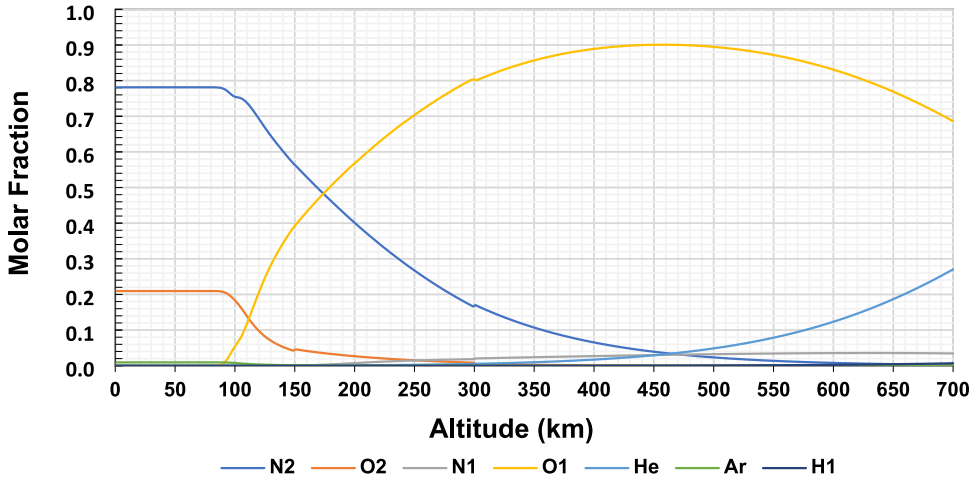

Fig. 5. Atmospheric Composition of the Default Case, vs Altitude. Composition expressed in Molar Fractions.

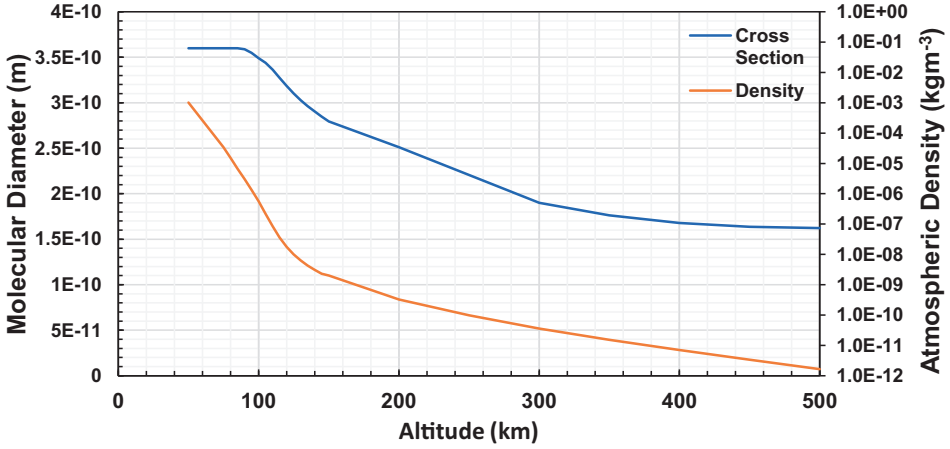

Fig. 6. Average Molecular Diameter of Atmosphere, and Atmospheric Mass Density of Default Case, vs Altitude.

wake region of the higher altitude cases. There exists a certain 'jaggedness' in the wake regions of each case – previous work has established that this is connected to the pattern of sampling points in the v-space discretisation, i.e. they are not real flow phenomena (Evans et al, 2011).

Peak number densities were also recorded and compared with free stream. The highest number densities occur at the leading edges of the CubeSat. Typically, the distribution was even across all leading surfaces, although absolute maximum occurs at the centre of the leading face of the on-axis case, and the same occurs for the protruding vertex of the off-axis case. Fig. 8 shows the maximum observed number density versus that of the free stream. It was assumed that the ratio of these number densities equates to the ratio of monoatomic oxygen particles. This would allow more insight into the rate of corrosion at these surfaces, as the density of oxygen is higher than the free stream, although the molecular wall reflection parameter, α (0.9 in the default cases) would also govern this.

Fig. 9 illustrates how the number density increases around the leading edges of the CubeSat. It is at 125 km altitude for the default case, showing both the on and off-axis cases.

As can be seen, the highest proportion of particles can be found at the leading edges. There also exist regions upstream of the CubeSat that have a higher density (on-axis case), as well as regions of higher density protruding perpendicular to the free stream (off-axis). The increased number of particles in these regions was due to reflection – particles that have already impacted the leading edges and have been reflected in response to the geometric angles.

Velocity distributions were also visualised. Fig. 10 illustrates the velocity flow fields, as well as including vector arrow to show local velocity directions. This was performed for the default cases at altitudes of 125 km and 400 km (for both on and off-axis configurations).

For both on-axis cases, maximum velocity observed was only slightly higher than the free stream. Stagnation occurs

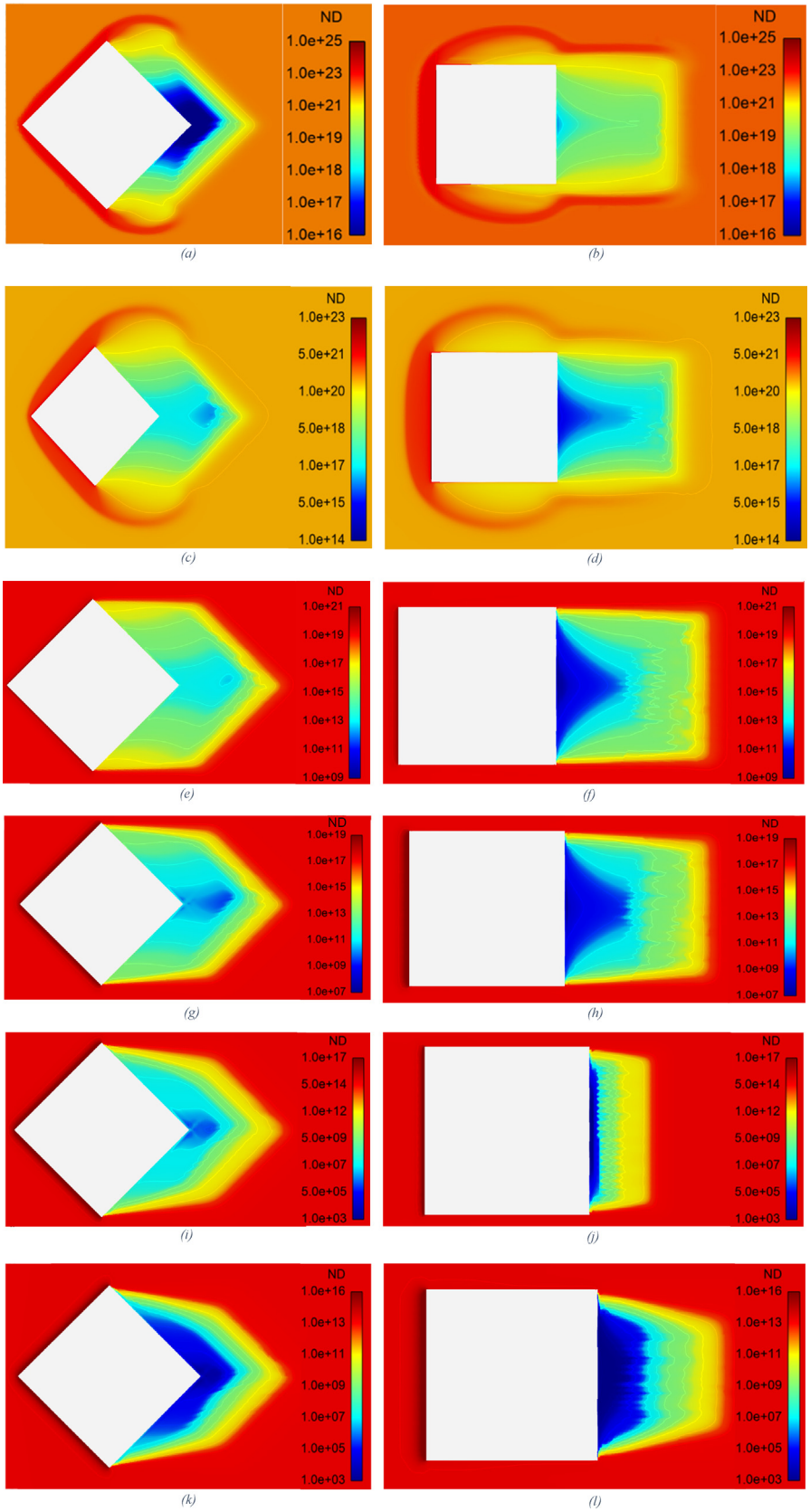

Fig. 7. Number Density (m^{-3}) distribution of atmosphere around the 1U CubeSat (0.1 m side length). Off-axis cases on the left, On-Axis cases on the right. All results are for the default case (1st April 1970 00:00, 45° lattitude, 180° longitude). Velocity equal to circular orbital velocity at each altitude. (a – b) corresponds to an altitude of 50 km. (c – d) = 75 km, (e – f) = 100 km, (g – h) = 125 km, (i – j) = 250 km, (k – l) = 400 km. Common palette levels for each altitude between on and off-axis cases to allow direct comparison. Contour sublevels set to 1.

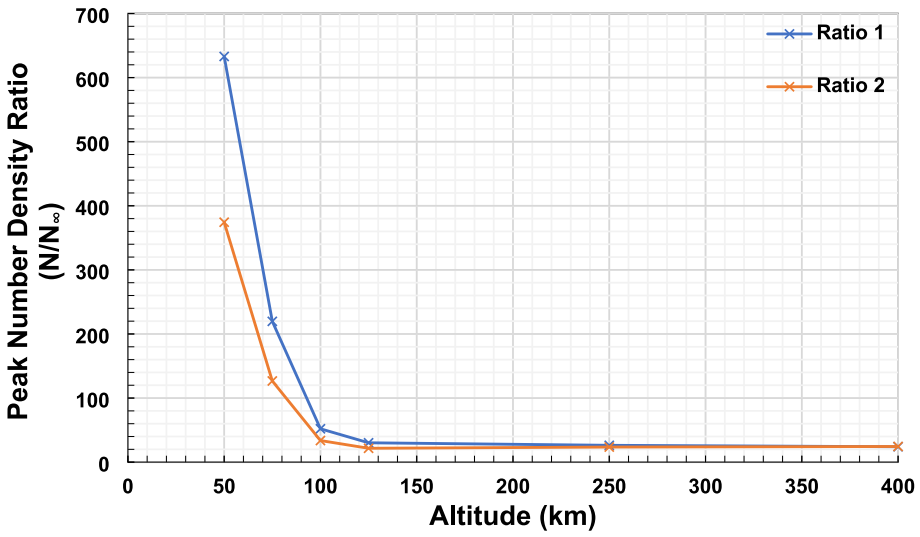

Fig. 8. Ratio of Peak Number Density to Free Stream Number Density. Both Cases Settle to a Ratio of 24. Ratio 1 is the on-axis case, Ratio 2 is the off-axis case.

at the leading edge of the CubeSat, and a region of lower velocity exists in front of the geometry. This correlates strongly with the number density distribution. The wake region exhibits a small stagnation point at its centre. The regions surrounding this show regions of moderate velocity. For the off-axis cases, the maximum velocity is observed in the wake regions. This velocity exceeds that of the free stream. It is proposed that the regions of lower number density (close to the trailing surfaces) have an influx of particles from the neighbouring regions of free stream density, creating a gradient. Via propagation of collisions, the free stream particles are accelerated from the high-density regions to the low-density regions. This occurs on both upper and lower trailing surfaces, and these local velocities merge at the trailing vertex.

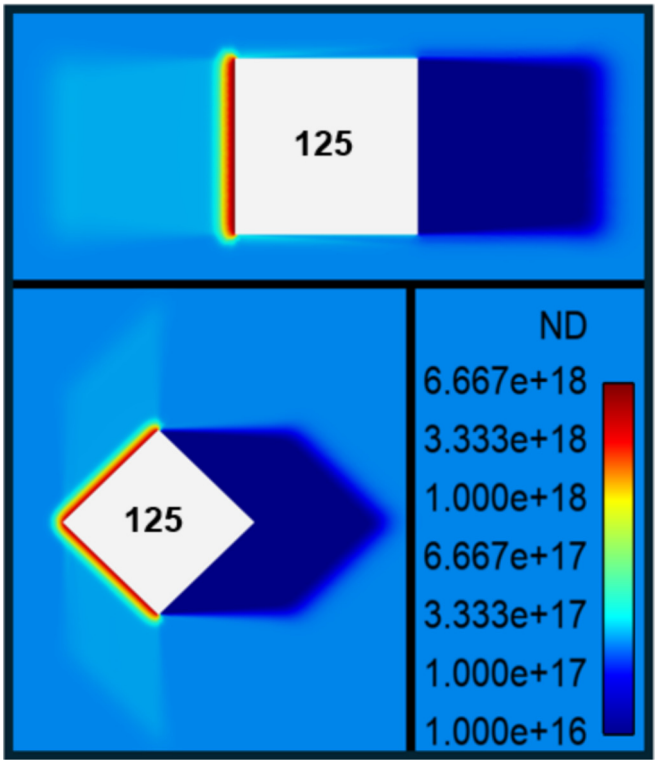

Fig. 9. Linear Scale Used to Show Number Density Distribution of the Leading Edges. Default Cases, 125 km.

3.3. Drag computations and drag coefficients

As the solver is two-dimensional, all drag coefficients were calculated using a reference length of 0.1 m (the typical length of a 1U CubeSat's edge). Off-axis cases also used this value for S to allow for intuitive comparisons of total drag when compared to the on-axis cases.

The value of C_D, the drag coefficient for three-dimensional analyses, was set to equal that of c_d, and the value of S for the three-dimensional cases was set to 0.01 m^2, corresponding to the two-dimensional frontal area. Again, the same area value was used for the off-axis cases' C_D. Fig. 11 below shows how c_d varied with altitude, for both the on and off-axis cases, as well as compared to the computed Knudsen number. Fig. 12 is provided of the same results, giving a clearer picture of lower altitudes.

Although minor variations of c_d occur, the on-axis cases settle to a value of around 1.24, whereas the off-axis cases tend towards a value of approximately 1.60. The larger frontal area of the off-axis cases was responsible for this at higher altitudes. The classical aerodynamic shape of the off-axis cases produces less drag only at altitudes where the atmospheric density was high enough to allow for near-continuum flow – starting to produce more drag around 88 km altitude. At such a low altitude, all satellites would experience unacceptably significant drag and thermal heating. As such, these altitudes were primarily computed to test the validity of the models. The most varied regions

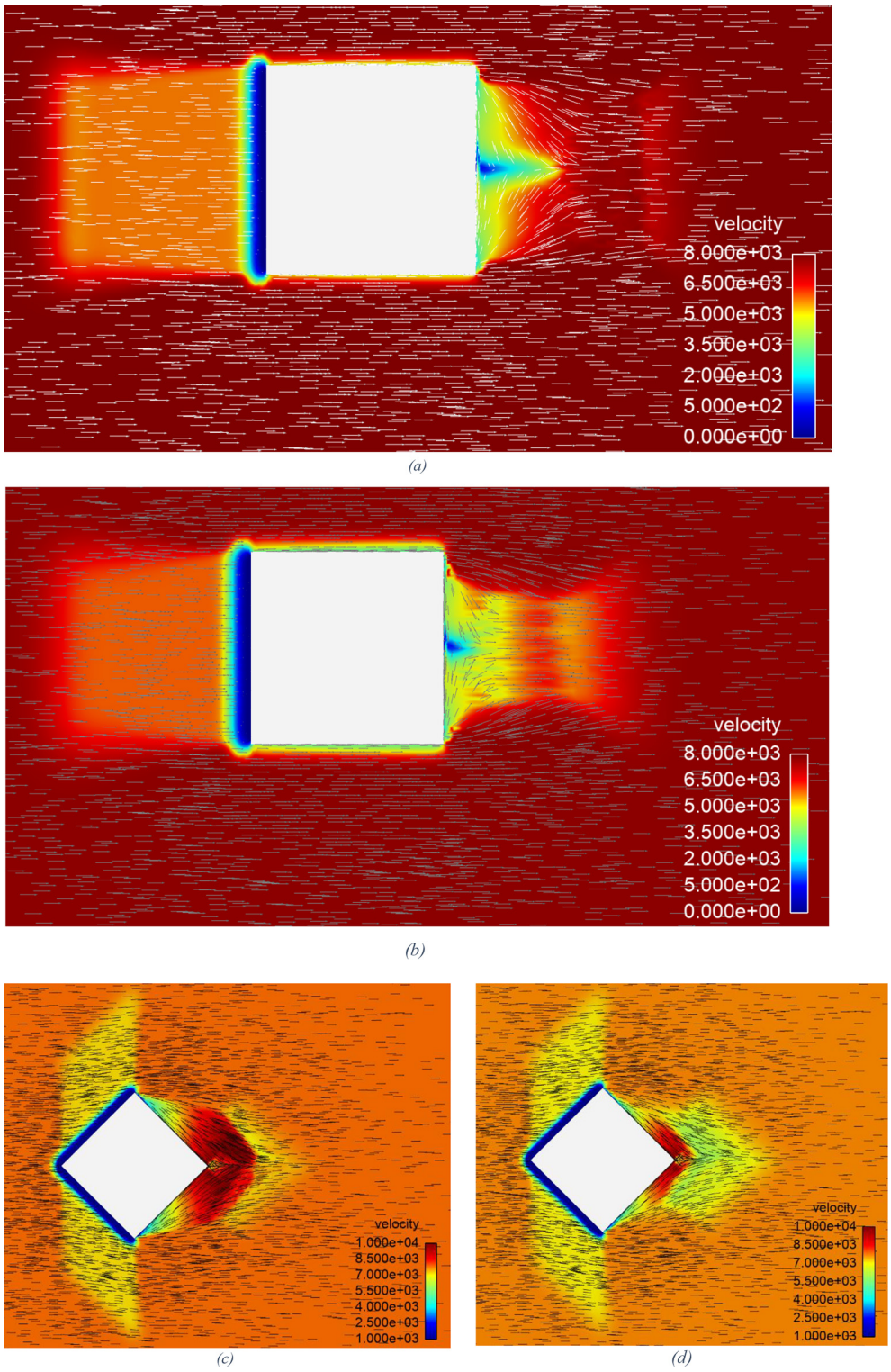

Fig. 10. Velocity distribution and vector arrows for the default cases. (a) 125 km altitude. On-axis case. $v_\infty = 7833$ ms^{-1}, $v_{max} = 7845$ ms^{-1}, $v_{min} = 4.5$ ms^{-1}. (b) 400 km altitude. On-axis case. $v_\infty = 7673$ ms^{-1}, $v_{max} = 7710$ ms^{-1}, $v_{min} = 7.4$ ms^{-1}.(c) 125 km altitude. Off-axis case. $v_\infty = 7833$ ms^{-1}, $v_{max} = 10416$ ms^{-1}, $v_{min} = 206$ ms^{-1}. (d) 400 km altitude. Off-axis case. $v_\infty = 7673$ ms^{-1}, $v_{max} = 9781$ ms^{-1}, $v_{min} = 195$ ms^{-1}.

of c_d occur around 75 – 110 km altitude for the default case. This corresponds to a Knudsen number of 0.02 – 10.7, consistent with the transitional regime of near-continuum to free molecular flow. Above these Knudsen numbers, the computed drag remains consistent, so drag was no longer considered a function of Kn.

Assuming the 3D drag coefficient, C_D, is equal to the two-dimensional coefficient, c_d, the 3D drag can be com-

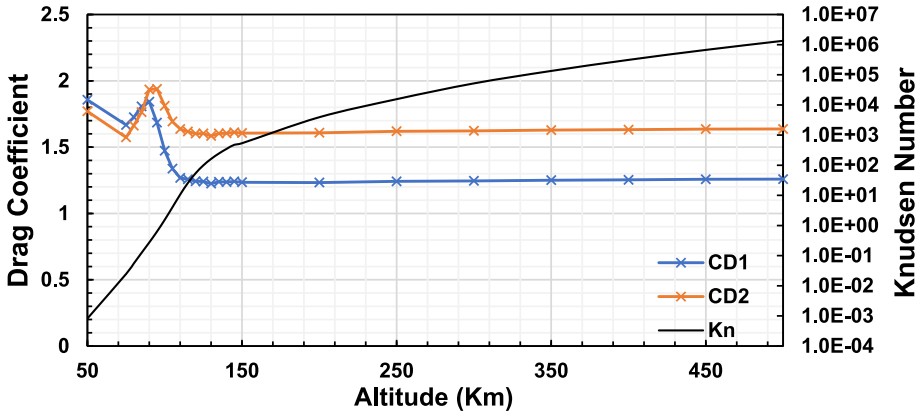

Fig. 11. 2D Drag Coefficient vs Altitude of the Default Case. CD1 Represents the On-axis Cases, CD2 is the Off-axis Cases.

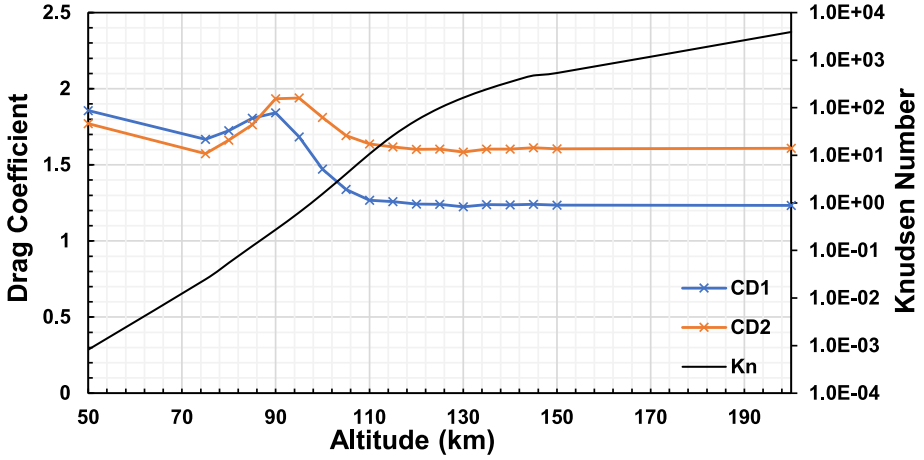

Fig. 12. The Same Results as the Fig. 11 but Highlighting the Lower Altitude Regions of Interest.

puted, using the same cases' free stream parameters. Fig. 13 displays the results.

The region between 100–200 km has a significant order of magnitude difference in the drag values. At 100 km, this was on the Newton level. At around 150 km, it was approximately 1mN, and at 200 km, approximately 0.1 mN. At 500 km the drag was calculated to be on the micro-Newton level, suggesting a relatively stable orbit and allowing an uncompensated system to have a significant lifespan. A high-specific impulse, low thrust electric propulsion system, such as an ionic liquid electrospray micro-propulsion unit (on the order of 10 μN per ~1 cm^3 unit) could effectively compensate drag for an altitude of about 350 km (Jenkins et al, 2018). These units can be arrayed, allowing for multiple micro-thrusters per CubeSat. An array consisting of approximately ten of these units could supply a thrust of around 0.1 mN. Thus, they could compensate for drag at approximately 200 km. Although there would be variations due to non-aerodynamic drag, wall reflection parameter differences of the surfaces, and geographical/temporal considerations (including periods of solar maxima), the drag is exponential to a degree where the altitude at which a thruster could compensate drag should be accurate to approximately 25 km to the computed results.

If the CubeSat is approximated to have an average drag coefficient equal to the average of the combined on-axis and off-axis cases, then the c_d would average at 1.42. This is substantially lower than the typical 2.0 – 2.2 value used for compact satellites, although large variance occurs in literature in both experimental and numerical models (Vries, 2010, Sun et al, 2021, Macario-Rojas, 2018, Murcia Piñeros et al, 2021). As this model only accounts for aerodynamic drag, the lower computed values therefore reflect the non-aerodynamic drag a satellite also experiences, including the effects of charged particles. Additionally, the wall reflection parameter, α, of 0.9 may be an overestimate of some satellites, although it is probable that any satellites designed to operate in VLEO would have dedicated coatings to help mitigate drag and reduce corrosion. Therefore, a value of 0.9 was presumed more representative of a CubeSat designed for operating in this harsher environment. Section 3.4 details the influence of the molecular

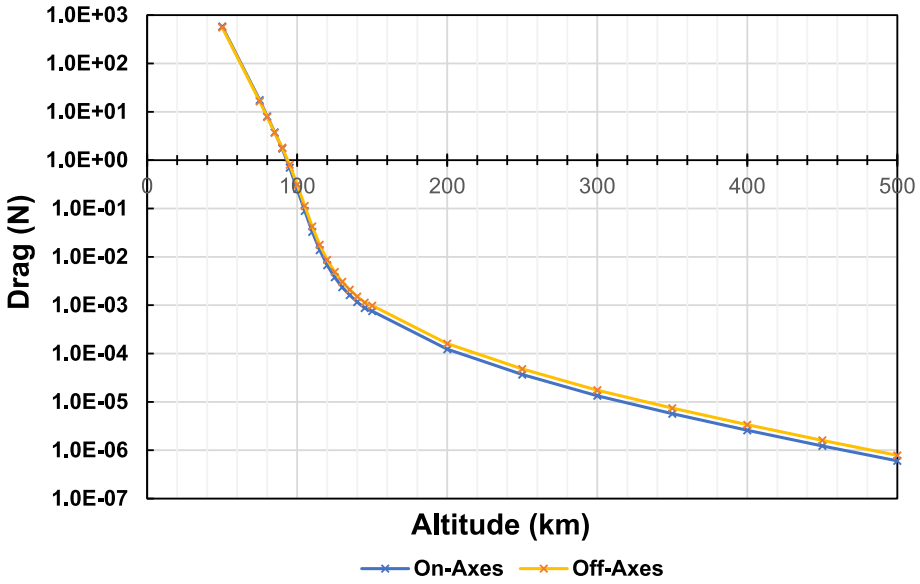

Fig. 13. Three-Dimensional Drag Computations vs Altitude for the Default Cases.

wall reflection parameter, including how altering its value encompasses the typical c_d range of 2.0–2.2.

3.4. Molecular wall reflection parameter studies

Multiple studies were conducted to evaluate the difference in c_d computed for varying values of α. The values of α were varied at 0.1 increments, from 0.1 to 0.99. This was conducted for both the on-axis case and off-axis case at altitudes of 125 km and 250 km. Fig. 14 shows the results of these simulations.

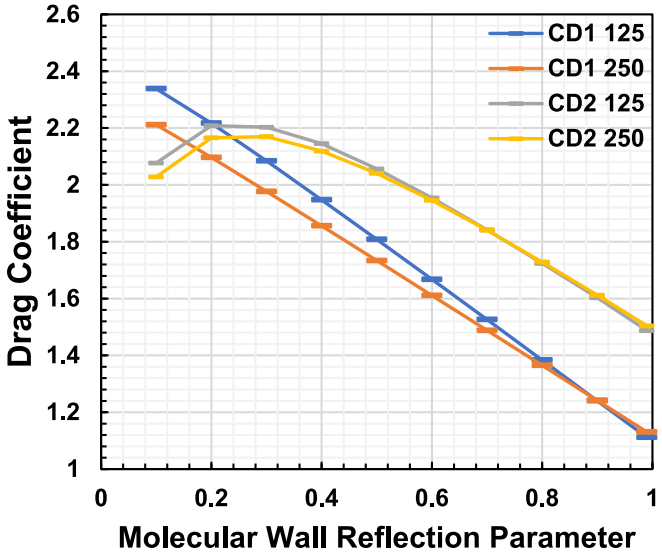

Fig. 14. Impact of the Molecular Wall Reflection Parameter α on Computed Drag Coefficients. CD1 Refers to a Drag Coefficient for the On-axis Case, Whereas CD2 is the Off-axis Case. 125 and 250 are the Altitudes Studied, in Kilometres.

For the on-axis case, the drag coefficient decreases near linearly as a function of α. A higher drag coefficient was produced at a lower altitude, however these values converge at an α value of approximately 0.9. For an α greater than this, the drag coefficient was lower for the 125 km case. For the off-axis cases, the function was more complex. For both altitudes studied, peak drag coefficients occur at an α value of approximately 0.2 – 0.25. It was unclear what causes the decreased drag coefficients of this configuration for a lower value of α, however it was likely caused by complex collisional phenomena. At an α of approximately 0.5, the drag coefficient calculated was equivalent to an α of 0.1. Both altitudes' drag coefficient converges at an α of 0.6. Any value of α higher than this causes the lowest drag coefficient, which was near identical (independent of altitude). Direct comparisons with other models, such as Direct Simulation Monte Carlo (DSMC) are challenging, due to the strong influence the wall reflection parameter has on the computed results. This parameter is specific to the Boltzmann-BGK process, and differs to the similar constructs used by DSMC termed 'accommodation coefficients' – these were are also found to have a strong influence on computed drag coefficients, however the accommodation coefficients dictate particle reflections more explicitly when compared with the wall reflection parameter (Hall, 2011, Crisp et al, 2022).

3.5. Geographic and temporal case studies

To compare the effects of differing orbital conditions, multiple studies were conducted. These include equatorial and polar orbits, periods of maximum and minimum solar irradiance, local winter/summer and local day (as opposed to local night, as with the default case). Table 1 below states the conditions of these cases.

Table 1
Summary of all geographic/temporal case studies, used to compare different conditions to the default cases. Used in Fig. 15.

Case Number	Description
0	Default Case - Medium solar irradiance, midnight, 45 degrees latitude, 180 degrees longitude, Spring. (1st April 1970)
1	Default Case - 0 degrees latitude
2	Default Case - 90 degrees latitude
3	Maximum solar irradiance case, midnight, 0 degrees latitude, 180 degrees longitude, Spring. (1st April 1990)
4	Maximum solar irradiance case - 45 degrees latitude
5	Maximum solar irradiance case - 90 degrees latitude
6	Minimum solar irradiance case, midnight, 0 degrees latitude, 180 degrees longitude, Spring. (1st April 1986)
7	Minimum solar irradiance case - 45 degrees latitude
8	Minimum solar irradiance case - 90 degrees latitude
9	Default Case - Midday
10	Default Case - Midday, winter (1st Jan 1970)
11	Default Case - Midday, summer (1st July 1970)

These cases give an overview of differing geographic and temporal conditions. This allows for different orbital pathways to be compared, as well as how the differing effects of solar irradiance may affect drag values. Fig. 15 show the calculated three-dimensional drag for these 11 cases. The first figure is for an altitude of 110 km (considered to be the absolute minimum altitude a propulsion enabled CubeSat could complete a single orbit in). The second is for the same cases but at an altitude of 200 km – considered an achievable stable orbit for many orbital periods, assuming adequate drag compensation and a high thruster specific impulse. The secondary axes of both figures show the mass density of the free stream, marked by a black X. The default case's drag computation is also illustrated with a dashed orange line, for comparison.

Free stream mass density is determined by many complex factors, including temperature and molar fractions of constituent particles. As such, there was no clear correlation between each geographic case and expected density. Typically, the period of solar maxima produced a higher mass density. Despite this, a local winter usually produced a higher density compared to a local summer. In general, the equatorial positions were observed to have a higher density compared to polar locations, although there were outliers to this trend. A 45° latitude typically falls between these two extremes, however that was not always a certainty.

For the 110 km case, the lowest drag value is 78.0% of the mean average of each case. The highest drag force was 117.4% the average value. For the 200 km case, the lowest value observed was 63.4% of the average drag force, while the maximum drag recorded was 131.4%. The highest drag value for both cases was Case 3 – an equatorial orbit during a period of solar maxima. Despite large fluctuations in absolute drag values, the drag coefficients remain significantly more consistent. For the 110 km case studies, the

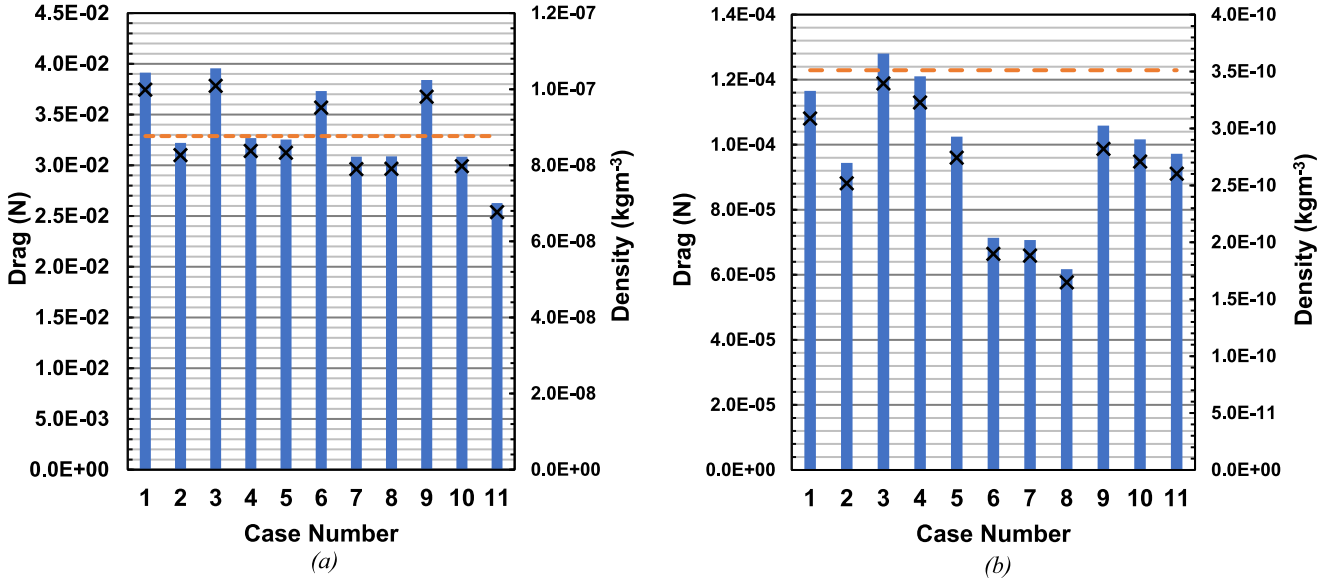

Fig. 15. Geographic Case Studies. Refer to Table 1 for Case Descriptions. Blue Bars Illustrate Drag (N). Black X's Mark Mass Density of Freestream. Orange Dashed Line Represents Default Case's Drag. (a) Altitude 110 km. (b) Altitude 200 km.

maximum c_d was 100.57% the value of the average, whereas the minimum c_d was 99.54%. For the 200 km cases, a maximum value of 100.46% was found, and the minimum was 99.09%.

Knudsen numbers of the 110 km cases were recorded as being as low as 9.0 (Case 3). Coupled with the very consistent drag coefficients, it was found that aerodynamic drag coefficients were independent of geographic and temporal conditions, for a given altitude. Despite this, free stream mass density varies considerably, so absolute drag (and therefore a drag-compensating propulsion system's thrust performances) must be evaluated, using the drag coefficients. It is also imperative to factor in the presence of non-aerodynamic drag – a significantly higher number of non-neutral species will be present during periods of solar maxima, when compared with solar minima, for example.

4. Conclusion

A VLEO 1U CubeSat has been simulated using a Boltzmann-BGK method for the first time. The computed aerodynamic drag coefficients should allow for approximate and preliminary impulse calculations of any satellite's orbital trajectory. The coefficients can also be coupled with existing models, to determine rate of decay of orbital altitude (Vries, 2010). The primary focus of this work was to evaluate drag values to design novel electric propulsion thrusters to compensate for drag. This allows a stable orbit, whereas a satellite lacking propulsion would quickly deorbit. Although circular orbital velocities were used in drag coefficient calculations, the coefficient remains near-constant above Knudsen numbers above approximately 10. Elliptical orbits have differing orbital velocities, but their instantaneous drag values should be able to be computed using the aerodynamic drag coefficient evaluations. This allows for orbits with a close perigee (for highest resolution Earth observation) and a distant apogee (allowing a large Dwell time for Earth observation). As such, the drag coefficients should be able to estimate the total impulse of an orbital period for circular and elliptical orbits. Along with a propulsion system's thrust performance and specific impulse levels, this will determine if a propulsion unit can effectively compensate for drag, as well as determining the mass of propellant required to achieve this for a given number of orbits, determined by design life.

As these studies only account for aerodynamic drag, it is recommended to apply a safety factor if used for sizing propulsion systems, to account for non-aerodynamic forces, including solar winds. Additionally, the molecular wall reflection parameter was shown to have a significant effect on the drag coefficient. This emphasises how dedicated drag reducing coatings may serve to substantially increase satellite service life, as well as reducing the propellant mass of drag compensation systems. Finally, monoatomic number densities have been evaluated. It was found that the number densities of the leading edges of the CubeSat were more than an order of magnitude higher than the free stream – a finding which may help guide oxygen corrosion analysis.

This research received no specific grant from any funding agency in the public, commercial, or not-for-profit sectors.

Declaration of competing interest

The authors declare that they have no known competing financial interests or personal relationships that could have appeared to influence the work reported in this paper.

References

Bahmani, S., Nazif, H.R., 2019. Erosion of oval elbows in turbulent particulate natural gas flow with different aspect ratio of cross-sections. Part. Sci. Technol. 39, 1–18. https://doi.org/10.1080/02726351.2019.1673856.

Banks, B.A., De Groh, K.K., Rutledge, S.K., 2019, Consequences of atomic oxygen interaction with silicone and silicone contamination on surfaces in low Earth orbit, NASA Technical Memorandum–1999-209179, Document Identification Number: 19990047772.

Baranger, C., Dauvois, Y., Marois, G., et al., 2020. A BGK model for high temperature rarefied gas flows. European Journal of Mechanics/B Fluids 80, 1–12. https://doi.org/10.1016/j.euromechflu.2019.11.006.

Bhatnagar, P.L., Gross, E.P., Krook, M., 1954. A model for collision processes in gases. I. Small amplitude processes in charged and neutral one-component systems. Phys. Rev. 94, 511–524. https://doi.org/10.1103/PhysRev.94.511.

Burth, R.H., Cathell, P.G., Edwards, D.B., et al, 2023, NASA Sounding Rockets User Handbook, NASA Technical Publication. NASA/TP–20230006855.

Chapman, S., Cowling, T.G., 1990. The mathematical theory of non-uniform gases: an account of the kinetic theory of viscosity, thermal conduction and diffusion in gases. Cambridge University Press.

Cnossen, I., 2022. A realistic projection of climate change in the upper atmosphere into the 21st century. Geophys. Res. Lett. 49. https://doi.org/10.1029/2022GL100693.

Crisp, N.H., Roberts, P.C.E., Hanessian, V., et al., 2022. A method for the experimental characterisation of novel drag-reducing materials for very low Earth orbits using the Satellite for Orbital Aerodynamics Research (SOAR) mission. CEAS Space Journal 14, 655–674. https://doi.org/10.1007/s12567-022-00434-3.

Deng, Z.T., Liaw, G.S., Chou, L.C., 1995, Numerical investigations of low-density nozzle flow by solving the Boltzmann equation, NASA Technical Memorandum, NASA-TM-110492.

Emmert, J.T., Drob, D.P., Picone, J.M., et al., 2021. NRLMSIS 2.0: a whole-atmosphere empirical model of temperature and neutral species densities. Earth Space Sci. 8. https://doi.org/10.1029/2020EA001321.

Evans, B.J., Morgan, K., Hassan, O., 2008, Finite element solution of the Boltzmann equation for rarefied macroscopic gas flows, PhD thesis, Swansea University. https://cronfa.swan.ac.uk/Record/cronfa42618.

Evans, B.J., Morgan, K., Hassan, O., 2011. A discontinuous finite element solution of the Boltzmann kinetic equation in collisionless and BGK forms for macroscopic gas flows. App. Math. Model. 32, 996–1015. https://doi.org/10.1016/j.apm.2010.07.027.

Evans, B.J., Walton, S.P., 2017. Aerodynamic optimisation of a hypersonic re-entry vehicle based on solution of the Boltzmann–BGK equation and evolutionary optimisation. App. Math. Model. 52, 215–240. https://doi.org/10.1016/j.apm.2017.07.024.

Evans, B.J., 2018. Nano–particle drag prediction at low Reynolds number using a direct Boltzmann–BGK solution approach. J. Comput. Phys. 325, 123–141. https://doi.org/10.1016/j.jcp.2017.09.038.

Evans, B.J., Hanna, M., Dawson, M., Mesiti, M., 2019. High order parallelisation of an unstructured grid, discontinuous-Galerkin finite element solver for the Boltzmann–BGK equation. Int. J. Computat. Fluid Dynam. 33, 343–351. https://doi.org/10.1080/10618562.2019.1651843.

Groesbeck, D.S., Hart, K.A., Gunter, B.C., 2019. Simulated formation flight of nanosatellites using differential drag with high-fidelity rarefied aerodynamics. J. Guid. Control Dynam. 44. https://doi.org/10.2514/1.G003871.

Hall, J., 2011. Advances in spacecraft technologies. InTech Publishing.

Harris, S., 1971. An introduction to the theory of the Boltzmann equation. Dover, Publications.

JAXA Press, 2019, Super Low Altitude Test Satellite (SLATS) "TSUBAME" has set a Guiness World Record, 24 December. https://global.jaxa.jp/press/2019/12/20191224a.html (accessed 14 February 2024).

Jenkins, M.G., Krejci, D., Lozano, P., 2018. CubeSat constellation management using ionic liquid electrospray propulsion. Acta Astronaut. 151, 243–252. https://doi.org/10.1016/j.actaastro.2018.06.007.

Kawasaki, H., Konoue, K., Hoshino, H., et al., 2018. Interim report of Super Low Altitude Satellite operation. IGARSS 4066–4069. https://doi.org/10.1109/IGARSS.2018.8517529.

Lemmer, K., 2017. Propulsion for CubeSats. Acta Astronaut. 134 (2017), 231–243. https://doi.org/10.1016/j.actaastro.2017.01.048.

Li, Z.H., Zhang, H.X., 2009. Gas-kinetic numerical studies of three-dimensional complex flows on spacecraft re-entry. J. Comput. Phys. 228, 1116–1138. https://doi.org/10.1016/j.jcp.2008.10.013.

Macario-Rojas, A., Smith, K.L., Crisp, N.H., Roberts, P.C.E., 2018. Atmospheric interaction with nanosatellites from observed orbital decay. Adv. Space Res. 61, 2972–2982. https://doi.org/10.1016/j.asr.2018.02.022.

Marín-Cebrián, A., Sebastião, I.B., Spencer, D.A., Tamrazian, S., 2019. DSMC-SPARTA aerodynamic characterization of a deorbiting CubeSat. AIP Conference Proceedings 2132. https://doi.org/10.1063/1.5119578.

Murcia Piñeros, J.O., Abrahão dos Santos, W., Prado, A.F.B.A., 2021. Analysis of the orbit lifetime of CubeSats in low Earth orbits including periodic variation in drag due to attitude motion. Adv. Space Res. 67, 902–918. https://doi.org/10.1016/j.asr.2020.10.024.

NASA, 2021, Community Coordinated Modeling Center, NRLMSIS 2.0 Instant Run Page, https://kauai.ccmc.gsfc.nasa.gov/instantrun/nrlmsis/ (accessed 11 February 2024).

Roberts, P.C.E., 2021. 1st Symposium of very low Earth orbit missions and technologies. CEAS Space Journal 14, 605–608. https://doi.org/10.1007/s12567-022-00466-9.

Sheridan, P.L., Paul, S.N., Avendaño-Franco, G., Mehta, P.M., 2022. Updates and improvements to the satellite drag coefficient Response Surface Modeling toolkit. Adv. Space Res. 69. https://doi.org/10.1016/j.asr.2022.02.044.

Sun, R., Riano-Rios, C., Bevilacqua, R., et al., 2021. CubeSat adaptive attitude control with uncertain drag coefficient and atmospheric density. J. Guid. Control Dynam. 44. https://doi.org/10.2514/1.G005515.

Vries, W.D., 2010, Cubesat Drag Calculations, Lawerence Livermore National Laboratory Technical Report 453771. LLNL-TR-453771.